Thermal / Pyrolysis Gas Flow Analysis of Carbon Phenolic Material

J. Louie Clayton
Thermodynamics and Heat Transfer Group
Marshall Space Flight Center / NASA
Redstone Arsenal, Alabama

ABSTRACT

Provided in this study are predicted in-depth temperature and pyrolysis gas pressure distributions for carbon phenolic materials that are externally heated with a laser source. Governing equations, numerical techniques and comparisons to measured temperature data are also presented. Surface thermochemical conditions were determined using the Aerotherm Chemical Equilibrium (ACE) program. Surface heating simulation used facility calibrated radiative and convective flux levels. Temperatures and pyrolysis gas pressures are predicted using an upgraded form of the SINDA/CMA program that was developed by NASA during the Solid Propulsion Integrity Program (SPIP). Multi-specie mass balance, tracking of condensable vapors, high heat rate kinetics, real gas compressibility and reduced mixture viscosity's have been added to the algorithm. In general, surface and in-depth temperature comparisons are very good. Specie partial pressures calculations show that a saturated water-vapor mixture is the main contributor to peak in-depth total pressure. Further, for most of the cases studied, the water-vapor mixture is driven near the critical point and is believed to significantly increase the local heat capacity of the composite material. This phenomenon if not accounted for in analysis models may lead to an over prediction in temperature response in charring regions of the material.

NOMENCLATURE

A -area
B' -dimensionless mass loss rate
C_H -Stanton Number, Heat Transfer
C_M -Stanton Number, Mass Transfer
C -specific heat
E -activation energy
F -1st generic coefficient
G -2nd generic coefficient
h -enthalpy
J -mass source/sink rate
k -thermal conductivity
K -permeability
m -mass
$\dot{m}$ -mass flow rate
mf -mass fraction
n -number of reactions
M -Molecular weight
P -total pressure
Q -heat transfer rate
R -gas constant
$\dot{s}$ -recession rate
S -source term
t -time
T -temperature
u -velocity
V -volume
w -weight fraction
x -spatial coordinate
z -compressibility factor
Z -diffusional driving potential
α -surface total absorptivity
β -pre-exponential factor
ε -surface total emissivity
Γ –resin volume fraction
μ -dynamic viscosity
ϕ -porosity
ρ -density
γ -coefficient for Forchiemer extension

Subscripts:
c -carbon
cn -condensation
e -edge
f -final
g -gas
i,j -free indices
o -original
p -constant pressure
r -recovery
rad -radiation
s -solid material
sc -solid conduction
t -total
v -virgin
vp -vaporization
w -wall

INTRODUCTION

The Space Shuttle Reusable Solid Rocket Motors (RSRM) have now provided the main propulsion source for over 95 missions. During this time a very extensive database of motor operational performance has been amassed which includes parameters such as nozzle insulation erosion rates. These data are understood statistically to the extent that variations on the order of tenths of an inch are indicators that a change has occurred in either materials and/or processes used in their refurbishment. The left hand nozzle of the RSRM-56 flight set displayed anomalous erosion (pocketing) aft of the throat (Fig. 1) affecting the full circumference of the motor and measuring as much as 0.5" deeper than expected mean values. Based on statistics, the event was approximately a 6-σ occurrence and thus could not be discarded without further understanding.

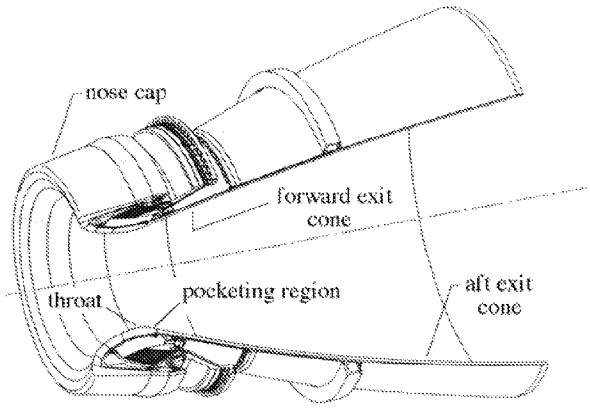

Fig. 1. RSRM Nozzle Showing Pocketing Region

The degraded material performance was believed to be attributable to the "pocketing" phenomenon that is distinctly different from typically occurring thermochemical erosion. At this location in the nozzle throat ring material ply angles are 45° to motor centerline and about 70° to the conducted isotherms. It is known that in-plane (with ply) fibers oriented orthogonal to the isotherms are more likely to pocket. It was therefore suspected that for the RSRM-56 nozzle, process variation had produced fiber orientations approaching 90° to the flame surface and was likely the primary cause of the increased erosion. Additionally, other factors related to materials and/or process variation were considered potential contributors thus it was decided to initiate a comprehensive test program aimed at gaining a better understanding of material thermostructural behavior.

The resources of the Laser Hardened Material Evaluation Laboratory (LHMEL) facility were utilized to examine pocketing activity as a function of fiber orientation and other material variations such as resin content, moisture content and ply distortions. LHMEL has the major advantages of a relatively large spatially flat surface heating distribution of precise magnitude, rapid turn-around test time and direct measurement of surface temperature. Disadvantages of the LHMEL are total pressures, thermochemistry and surface recession does not compare well with the actual RSRM. Average recession rates are about one-forth of that experienced in the RSRM nozzle at the location of interest. There is some debate and conflicting data [1] that seems to suggest that the effect of active surface thermochemistry may be important in terms of suppression of pocketing. Notwithstanding these data, the decision was made to test at LHMEL based on the belief that pocketing is an "in-depth" phenomena and not strongly dependent on surface recession.

The following provides a description of modifications incorporated into the SINDA/CMA computer code which was developed by the author [2] during the Solid Propulsion Integrity Program (SPIP). Upgrades include multi-specie mass balance, real gas equation of state using generalized compressibility data, reduced mixture viscosity, resin weight fraction Arrhenius formulation, high rate TGA coefficients and a condensation/ vaporization simulation for vapors in the pyrolysis gas mixture. Basic formulations of the energy and momentum equations remain essentially unchanged but will be covered for completeness.

Governing Equations

In-depth temperature and pyrolysis gas pressure calculations are based on simultaneous solution of 1-D conservation equations for mass, momentum and energy along with a real gas equation of state and kinetic rate equation. The following basic assumptions were incorporated into the math model:

1) Local thermal equilibrium exists between pyrolysis gas and solid thus one energy equation can describe thermal response of both.
2) Pyrolysis gas motion is governed by the Darcy-Forcheimer equation. Permeability and porosity data was correlated as a function of degree of char. Data was assembled from Clayton[3] and Stokes[4].
3) Temperature and pressure gradients are 1-dimensional thus material anisotropy can be simulated by use of effective properties. Rule of mixtures was used for determination of properties in the charring region.
4) Transport of condensable species through the pore network occurs in the vapor phase. Liquid occupying pore volumes was assumed to be stationary and in equilibrium with its respective vapor in the mixture. Condensation and vaporization rates are governed by the amount of a specie that can be thermodynamically accommodated in the mixture relative to saturation over a given time step.
5) Condensed phase species residing together in a pore volume are assumed not to interact with each other chemically or physically. Gas phase permeability remains unchanged due to the presence of liquid in the pore volumes.
6) Mixture specie concentrations, in the pore free volumes, were determined by "origin" generation, condensation/vaporization rates and upstream advection. Equilibrium and/or kinetic rate reactions within the gas and reactions with the char layer are currently not modeled.

Surface Energy Balance

Surface heating conditions are determined by consideration of combined convective, radiative and thermochemical loading. The LHMEL is unique, and different from the RSRM in that surface response is driven by the incident radiation emitted from a CO_2 laser and is convectivly cooled by air flow. Oxidation of carbon in the char layer is present and averages about one mil/sec depending on incident heat rate and location on the sample. Components of the surface heat flux are depicted in Fig. 2.

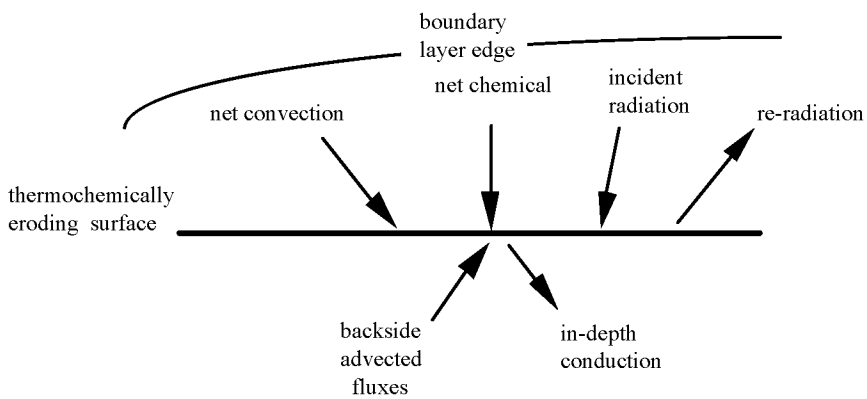

Fig. 2. Thermochemically Eroding Surface Boundary Conditions

During testing, surface radiometer data was collected and used for model calibration of surface optical properties. Backfitting model response to measured data across the range of incident flux levels, surface absorptivity was found to be independent of temperature while re-radiated energy levels were controlled by a temperature dependent emissivity. The backfit suggested that $\alpha \sim 0.97$ and ε was ~ 0.85 @ 3000°F and increased linearly to ~ 0.96 @ 5000°F. Forced convective cooling of the sample was imposed by a 0.5 Mach air flow directed parallel to the heated surface. Facility airflow calibration data was used for determination of convective heat and mass transfer coefficients and average values of these quantities input into the SINDA/CMA model. Surface oxidation rate was correlated in familiar b-prime table format and estimated by an ACE [5] solution for standard air environment. Surface recession rates average about one

mil/sec and vary substantially along the heated surface with the leading edge having the greatest erosion. Arithmetic summation of respective fluxes identified in Fig. 2. gives the following expression for the surface energy balance:

$$\rho_e u_e C_H \left(h_r - h_{e_w}\right) + \rho_e u_e C_M \left[\sum \left(Z_{i_e}^* - Z_{i_w}^*\right) h_i^{T_w} - B' h_w\right] + \dot{m}_c h_c + \dot{m}_g h_g + \alpha_w q_{rad} - F\sigma\varepsilon_w T_w^4 - q_{sc} = 0 \tag{1}$$

Terms left to right are identified as free stream convection, surface thermochemical, backside advective fluxes, radiation incident/emitted and conduction into the material. Numerical solution for the surface energy balance[2] is implicit with respect to temperature calculations but explicit in time relative to mass flow calculated quantities. Net flux values are loaded into the source term of the surface node during iterative convergence of the global temperature and pressure calculations. This numerical method is different from the standard CMA approach but the two methods compare well with a difference of less than 1/2 % in computed surface temperature[2].

In-Depth Thermal Solution

Invoking the assumption of gas-solid equilibrium, leads to the standard CMA[6] formulation for energy conservation given by Eq. 2. For this study an additional term that accounts for pyrolysis gas capacitance has been added to the equation per the general formulation provided by Keyhani [7]. Inclusion of gas capacitance has heretofore been considered unnecessary due to order of magnitude considerations however based on findings presented in this study, it is believed this term can become significant in charring regions of the material. Terms left to right are energy storage, conduction, decomposition, grid movement, pyrolysis gas flow and latent phase change rates. The last two terms were added to account for the phase energy of saturated water and phenol compounds.

$$\left(\rho_s C_s + \phi \rho_g C_g\right) \frac{\partial T_s}{\partial t} = \frac{1}{A} \frac{\partial}{\partial x}\left(kA \frac{\partial T}{\partial x}\right) + \left(h_g - \bar{h}\right) \frac{\partial \rho}{\partial t} + \dot{s} \rho C_p \frac{\partial T}{\partial x} + \frac{\dot{m}_g}{A} \frac{\partial h_g}{\partial x} + Q_{cn} - Q_{vp} \tag{2}$$

A finite element scheme was used for discretization of the energy equation. The computational grid consist of one dimensional first order elements with applied front/back face boundary conditions, Fig. 3.

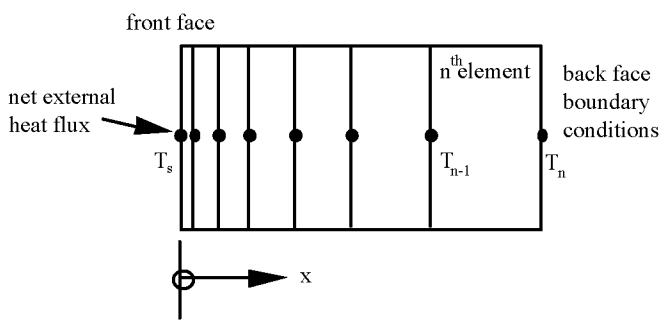

Fig. 3. One Dimensional Finite Element Grid

Surface recession is accommodated by movement of the grid relative to a fixed coordinate and applying a correction term to account for the induced advected energy into the element(s). As with the baseline CMA technique, the last element (furthest from the heated surface) shrinks to accommodate surface recession. If eroded total depth exceeds elemental thickness it is dropped from the active network and the adjacent element now absorbs the recession and so on. Determination of the elemental "stiffness" matrix is based on trapezoidal rule numerical quadrature which evaluates material heterogeneous and temperature dependencies explicitly in time. Temperature and pressure elemental integration points are coincident with a density field "nodlet" grid. Use of a nodlet grid for the density calculations is similar to the CMA technique and is generally necessitated by the exponential behavior of the Arrhenuis equation.

In-Depth Pyrolysis Gas Pressure Solution

Pyrolysis gas pressure distributions are calculated using a Darcy-Forcheimer form of the momentum equation substituted into the conservation of mass equation. Real gas effects for the mixture are simulated by application of a generalized compressibility factor to the ideal gas law. Pseudocritical temperatures and pressures[8] are calculated for the mixture based on mole fractions and the individual specie data. These "reduced" properties are used as independent variables for table lookup to determine the z factors. Mixture viscosity calculations[9] incorporate the effects of pressure, temperature and molecular polarity and are functions of mole fraction data and the pseudocritical reduced properties. Expression of gas properties in terms of mixture equivalents, i.e., gas constant, viscosity's, etc., permits use of Darcys equation for computation of total gas pressures. Specie partial pressures are simple functions of the mole fraction data which result from the multi-component mass balance. Terms left to right in Eq. (3) are functionally identified as gaseous mixture storage, total diffusive mass flux, total rate of pyrolysis gas generation, coordinate set movement correction, total multi-specie vaporization and condensation.

$$\frac{\partial}{\partial t}\left(\frac{\phi MA}{zRT}P\right) = \frac{\partial}{\partial t}\left[\left(\frac{K}{\mu\gamma}\right)(\rho_g)A\frac{\partial P}{\partial x}\right] - A\frac{\partial \rho_s}{\partial t} + \dot{s}\frac{\partial(\phi\rho_s)}{\partial x} + J_{vp} - J_{cn} \tag{3}$$

Eq. (3), the "pressure" equation, is analogous in formulation to the energy equation and is thus numerically solvable by the same finite element techniques used for temperature calculation. Assembly of the pressure elemental stiffness matrix relies on explicit quadrature of spatially dependent properties using the same procedure derived for the thermal calculations. Details of discretization of the diffusive term, treatment of source/sink terms and numerical degree of coupling are developed and discussed in Ref. [2].

In-Depth Kinetic Decomposition

A resin based weight fraction formulation of the Arrhenius equation was employed for the in-depth material decomposition simulation. Kinetics coefficients were developed by Clayton[10] and computed from high rate TGA data derived by Southern Research Institute (SoRI). The weight loss curve fit considered three reactions and was based on the 3000°C/minute data. The Arrhenius relationship used in the SINDA/CMA code has the following form:

$$\frac{dw_i}{dt} = \sum_{i=1}^{n} -w_{o_i}^{1-n_i}\left(w_i - w_{f_i}\right)^{n_i}\beta_i e^{\frac{-E_i}{RT}} \tag{4}$$

A thermal decomposition "nodlet" grid was implemented for refined description of variation in material density along the 1-D coordinate. This grid is fixed and contains time based composite material density resulting from integration of Eq. (4). A simple Euler scheme was applied in which integration time steps are set equal to the transient solution time step for the temperature and pressure calculations. Updating of temperature in the calculation occurs explicitly and the resultant pyrolysis gas flow rates are used explicitly in temperature and pressure calculations (loosely coupled). Quadrature involved in evaluation of stiffness matrices assumes a piecewise linear distribution of density described by integration of Eq. (4) at the fixed nodlet sites. Conversion of resin weight fraction data to composite density was based on the following relationship

$$\rho_s = \Gamma\rho_v\left(\sum_i w_i\right) + (1-\Gamma)\rho_v \tag{5}$$

Multi-Component Mass Balance

A multi-component mass balance allows for tracking of individual molecular species evolved during the in-depth thermal decomposition process. The procedure utilizes a control volume aligned with elements in the pressure grid, Fig. 4. Total rate of decomposition and thus pyrolysis gas generation is determined by Eq. (4) and is assumed strictly a function of temperature and local char state. Mole fraction data that describes molecular species evolved as a function

of degree of char taken from Clayton[3] was used to determine the "origin" generation rate. A total of eight molecular species were considered; water, carbon dioxide, carbon monoxide, methane, hydrogen, phenol, cresol and xylenol. Of these eight, water and phenol have critical temperatures high enough and occur in sufficient concentrations that condensation and vaporization has to be considered if accurate total pressure magnitudes are to be calculated.

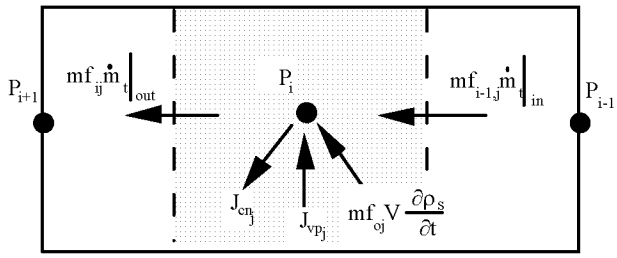

Fig. 4. Multi-Component Mass Balance

At the boundaries of the control volume are the advected fluxes of the individual species. Depending on computed direction of flow upstream contributions contribute to a weighted average type calculation of pore volume specie concentration. Equivalent molecular weights, gas constants, mixture viscosity's, specific heats are all functions of the mixture mole fraction calculations. Tracking partial pressures of individual species allows for simulation of condensation and vaporization. The computational procedure involves comparing specie partial pressure to its saturation pressure for the local temperature, Fig. 5. Below critical temperatures for the given specie, if its partial pressure tries to exceed the saturation pressure, an instantaneous rate of condensation is calculated that will keep the specie partial pressures equal to its saturation pressure (T_3' to T_3). Time integration of the rate of condensation gives the total amount of liquid that has accumulated in the open pore volumes. This liquid is available for vaporization when conditions are such that the mixture can thermodynamically accommodate its presence. Vaporization rates are computed based on the premise that the gas mixture remains saturated until all the liquid in the pore volume is removed(T_5' to T_5). Above critical temperatures gas mixture PVT behavior is described by the ideal gas law using generalized compressibility factors. The technique employed is similar to that used by Clayton[3].

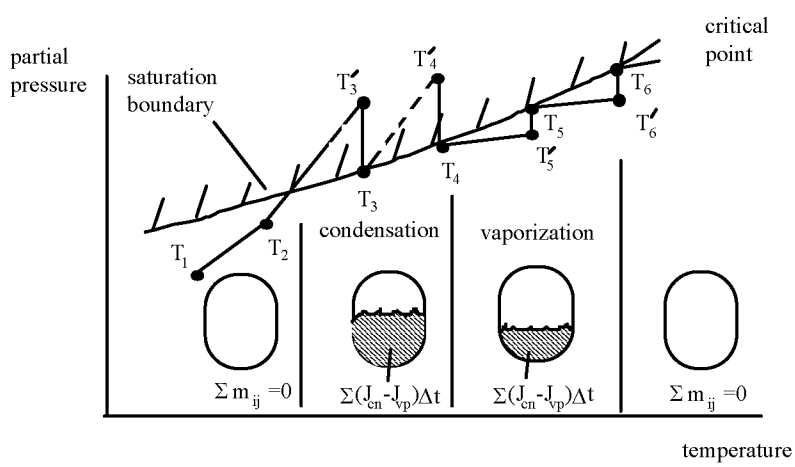

Fig. 5. Condensation and Vaporization Simulation

NUMERICAL SOLUTION

As previously discussed, discretization of energy and mass conservation equations was based on a finite element formulation employing a nodlet grid for integration of the Arrhenius equation. Time integration of the non-steady behavior of the diffusion equations, i.e., pressure and temperature, was performed by a Crank-Nicholson procedure. Eqs. (2) and (3), are cast into the following generic form:

$$F_i \frac{\Delta\Phi_i}{\Delta t} = \sum G_{ij}\left(\left(\Phi_j + \frac{\Delta\Phi_j}{2}\right) - \left(\Phi_i + \frac{\Delta\Phi_i}{2}\right)\right) + S_i \qquad (5)$$

where; Φ is temperature or total pressure

Eq. (5) is solved by iteration for the dependent variable $\Delta\Phi_i$. A successive point (Gauss-Seidel) scheme is applied which uses dependent and source term damping. Coupling is fully implicit between pressure, temperature and surface energy balance meaning that all quantities are converged together along with their respective coefficients and source terms at every time step. The Arrhenius equation is not iterated with temperature and pressures. A simple explicit updating is performed using "old" time step data values. The global method of solution is described in detail by Clayton[2] but will be summarized here to include the phase change logic. The overall numerical procedure goes as follows:

1) Initialize temperature, pressure, density and nodal coordinates. Compute coefficients in Equation (5).
2) Increment boundary information and solve for temperatures and pressures by iteration.
3) Using converged data in Variables 2, interpolate temperatures onto density grid and integrate Arrhenuis equation across the time step. Store decomposition data into an array versus position.
4) Recalculate coefficients in Eqn. (5) based on new properties data, i.e., conductivity's, permeability's, mass-energy source and sink rates, coordinate system location, etc...
5) Perform nodal mass balance as function of converged flow conditions for current time step. Compute mass and mole fractions, partial pressures, mixture equivalent properties.
6) Compare partial pressures with saturation pressure @ temperature for condensable species. If partial pressure is greater, using real gas law compute amount of mass removal necessary to make the two equal. Accumulate this mass as liquid in the control volume. If partial pressure is less than saturation, using real gas law compute amount of mass necessary to saturate mixture and vaporize accumulated liquid (if there is any). Adjust mass source terms in pressure network to reflect local rates of condensation/vaporization.
7) Perform grid movement logistics, if current time is less than end time return to step #2

Steps #3-#7 are performed in Variables 2 of the SINDA/CMA model thus all procedures described in these steps are explicitly coupled in time to the pressure and temperature calculations in step #2.

RESULTS

Spatial distributions for in-depth temperature and pyrolysis gas pressure for various incident radiant heating rates are presented in Figs. 6-14. For these cases ply angles are fixed at 90° and time slices at 3, 10 and 20 seconds are provided. For clarity, partial pressures of only major contributors such as water vapor, carbon dioxide and monoxide are presented. For the 300 Watt case, surface temperatures range from 2900°-3700°F and increase monatonically during the test. Peak total pressures range from 140-180 atmospheres with the maximum occurring at the 10 second time slice. Water vapor is the dominant pyrolysis gas specie in the charring regions of the material with mixture mole fractions approaching 99%. Gas flows are driven in-depth and to the heated surface depending on proximity relative to the peak pressure location. In the cooler material, carbon dioxide becomes the dominant specie. As the mixture is driven in-depth, the water vapor is condensed out leaving only species with critical temperatures low enough to exist as a gas at the given total pressure and temperature. For the 500 Watt cases, Figs. 9-11, surface temperatures range from 3600°-4300°F, increasing during the test. Peak total pressures range from 130-190 atmospheres with the maximum occurring at 3 seconds (earlier in test compared to 300 Watts). Specie distributions follow the same general trends. Looking at the 1000 Watt cases, Figs. 12-14, surface temperatures now vary from 4600°-5100°F and increase during the test. Peak total pressures range from 200-220 atmospheres with the maximum occurring at 10 seconds. Clearly observable trends in Figs. 6-14 are overall increase in material temperatures and total pressures with increasing surface heat flux.

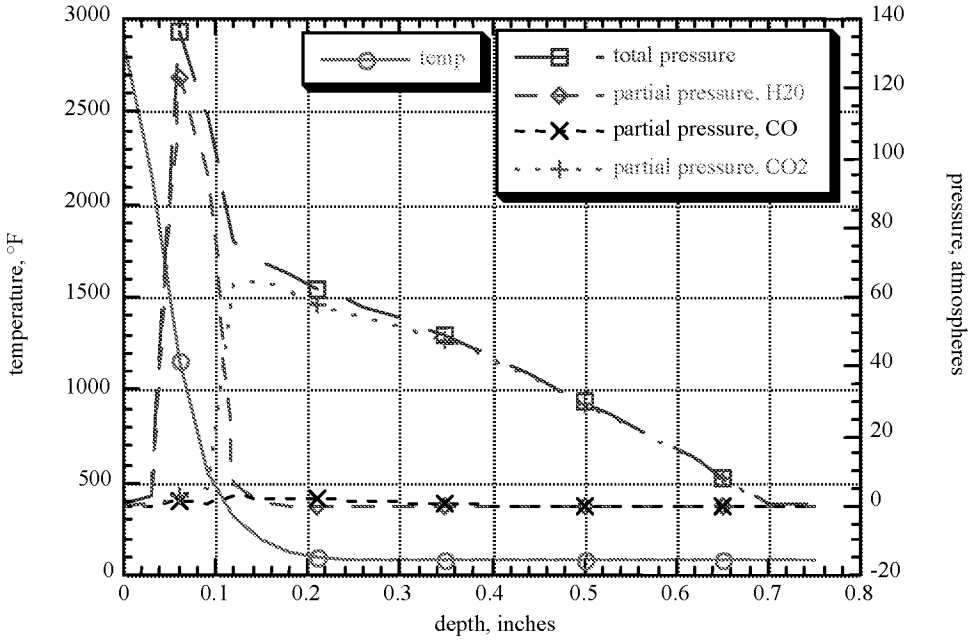

Fig. 6. Temperature and Pressure Distributions @ 3 Seconds
300 Watt Case, 90° Ply

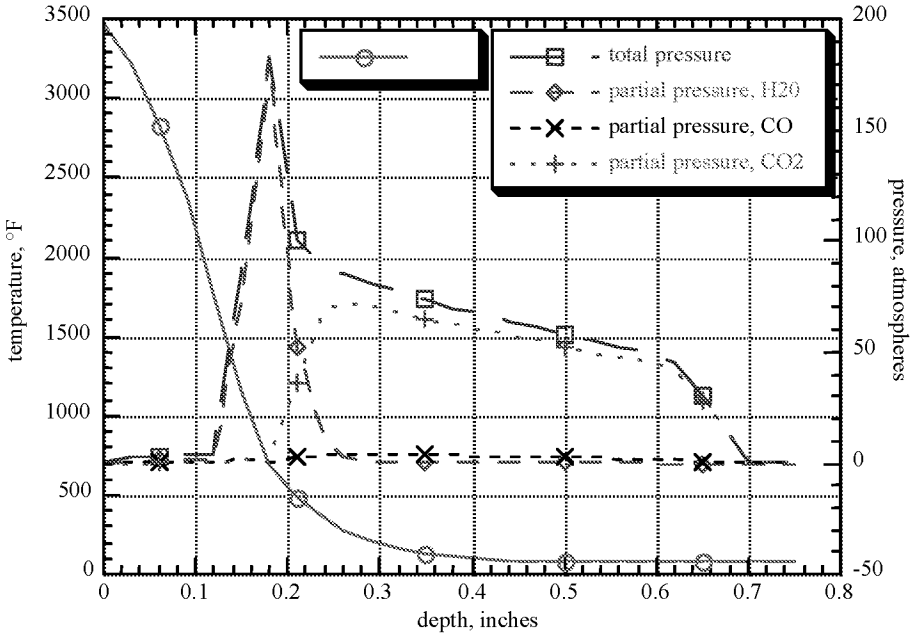

Fig. 7. Temperature and Pressure Distributions @ 10 Seconds
300 Watt Case, 90° Ply

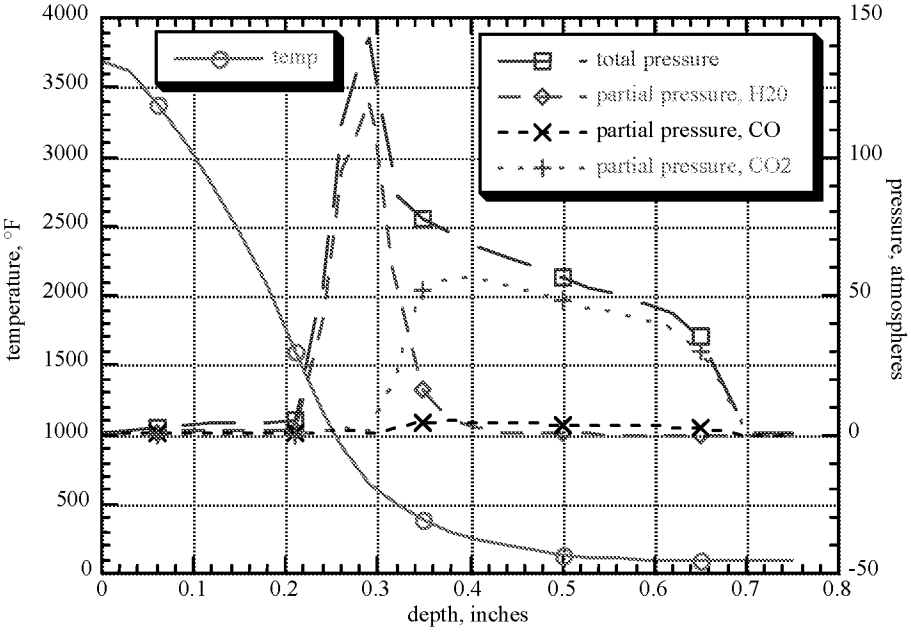

Fig. 8. Temperature and Pressure Distributions @ 20 Seconds
300 Watt Case, 90° Ply

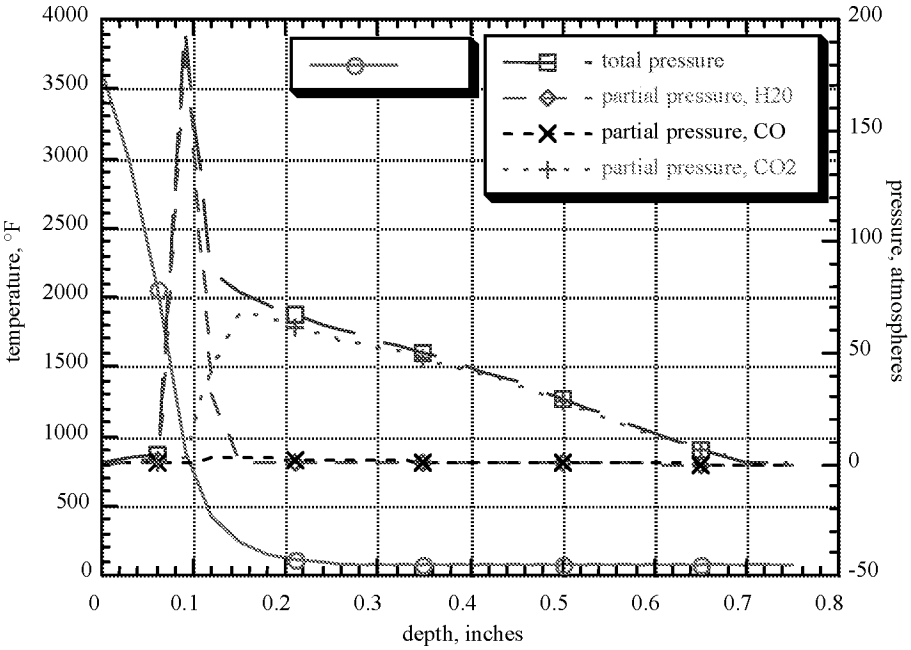

Fig. 9. Temperature and Pressure Distributions @ 3 Seconds
500 Watt Case, 90° Ply

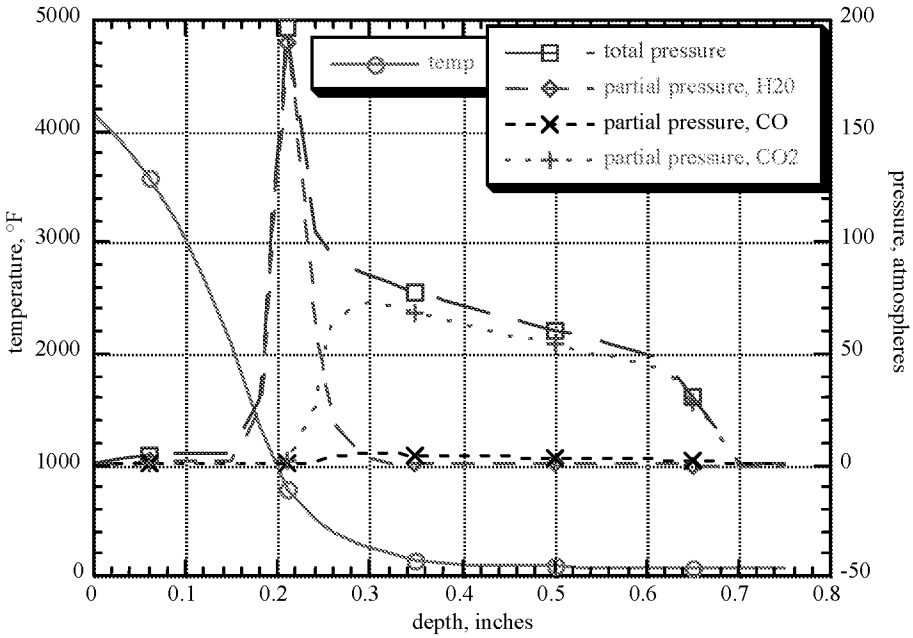

Fig. 10. Temperature and Pressure Distributions @ 10 Seconds
500 Watt Case, 90° Ply

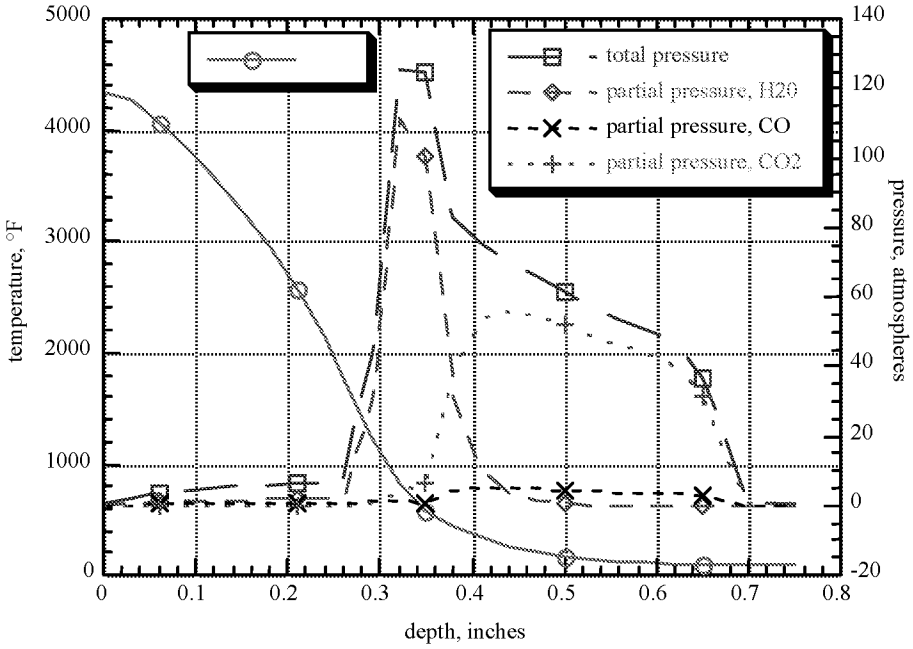

Fig. 11. Temperature and Pressure Distributions @ 20 Seconds
500 Watt Case, 90° Ply

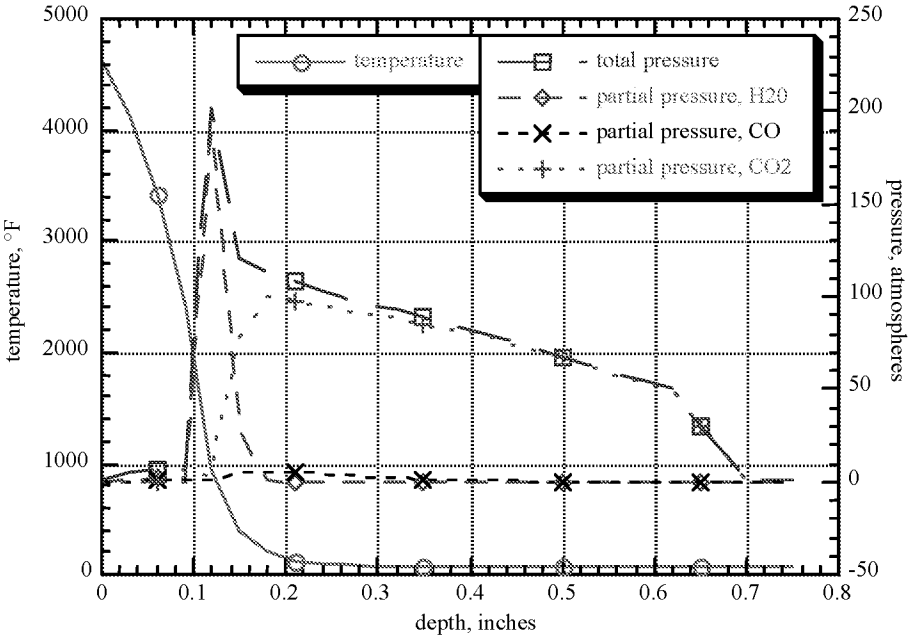

Fig. 12. Temperature and Pressure Distributions @ 3 Seconds
1000 Watt Case, 90° Ply

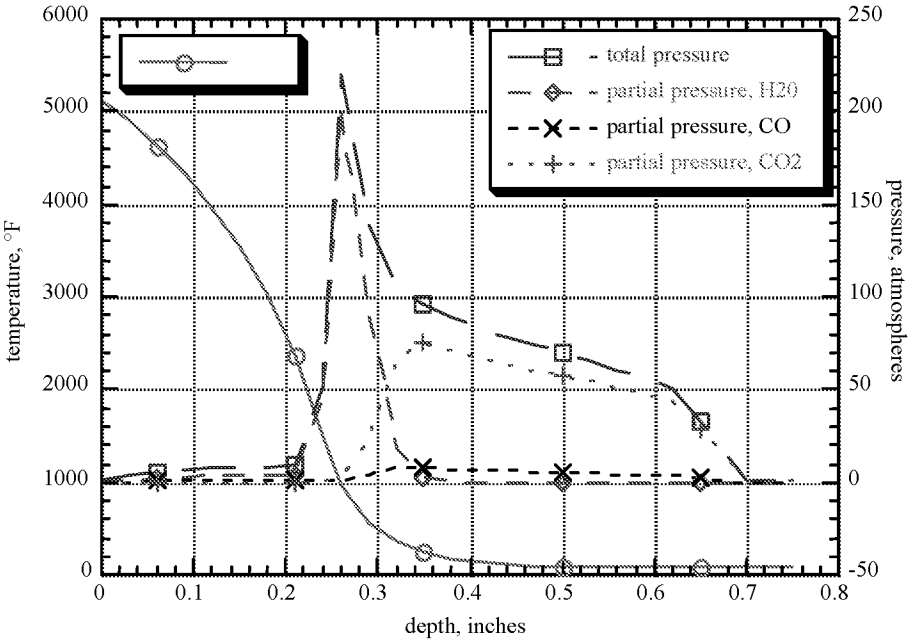

Fig. 13. Temperature and Pressure Distributions @ 10 Seconds
1000 Watt Case, 90° Ply

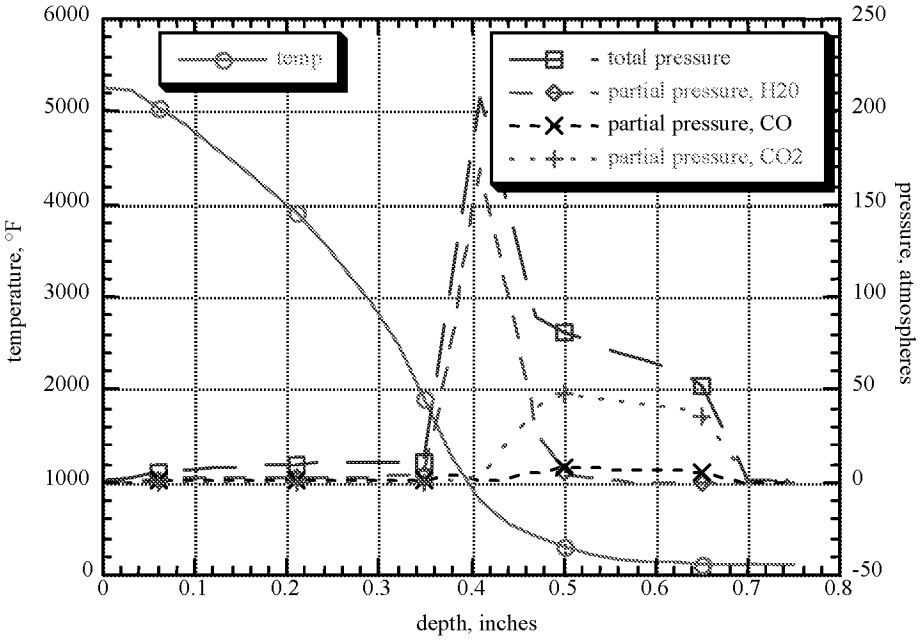

Fig. 14. Temperature and Pressure Distributions @ 20 Seconds
1000 Watt Case, 90° Ply

Provided in Figs. 15 and 16 are comparisons of predicted material thermal response to the laboratory measured data. Surface temperature data was obtained by radiometry while in-depth measurements were gathered by secondarily bonded thermocouples. Thermocouple depths were 0.125, 0.250 and 0.375 inches; a constant spacing of one-eighth inch. Adjustment of surface optical properties, per the discussed procedure, allowed for very good correlation in predicted response to the measured data. A good temperature match at the surface is a necessary starting point for understanding comparisons made at the in-depth locations. In general, the in-depth calculated quantities compare well with measured data and some discernible trends were evident. For the 300 Watt case at the 0.25" location, the measurement strays from the prediction at ~10 seconds. Comparisons at locations on both sides of this thermocouple are very good thus it is believed that the measurement may be inaccurate to some extent. High surface heating rate (1000 Watt case) comparisons are provided in Fig. 16. Unfortunately, lower capability thermocouples were used for this test and the in-depth measurements fail at ~2100°F. A general tendency for this test, and others in a series of ~1100 tests, is that model predictions lead measurements in the 700-1500°F range. Laboratory measured specific heats, for virgin and char material, were used for results presented in Figs. 15 and 16 to demonstrate this over prediction trend. Addition of saturated water pressure and temperature dependent specific heats into the energy equation would produce a better temperature comparison at the in-depth locations.

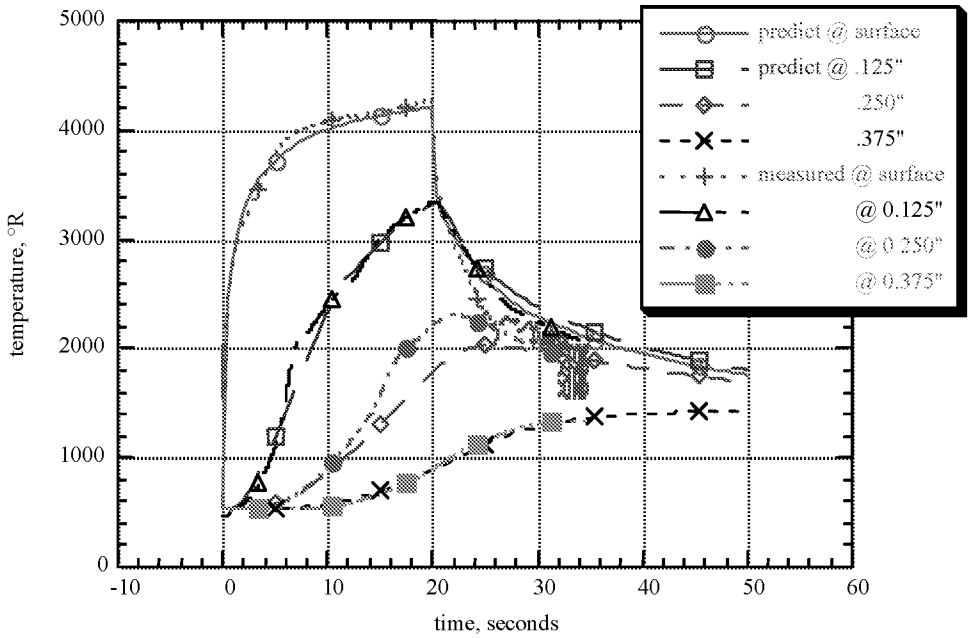

Fig. 15. Temperature Prediction versus Measured Data
300 Watt Case, 90° Ply

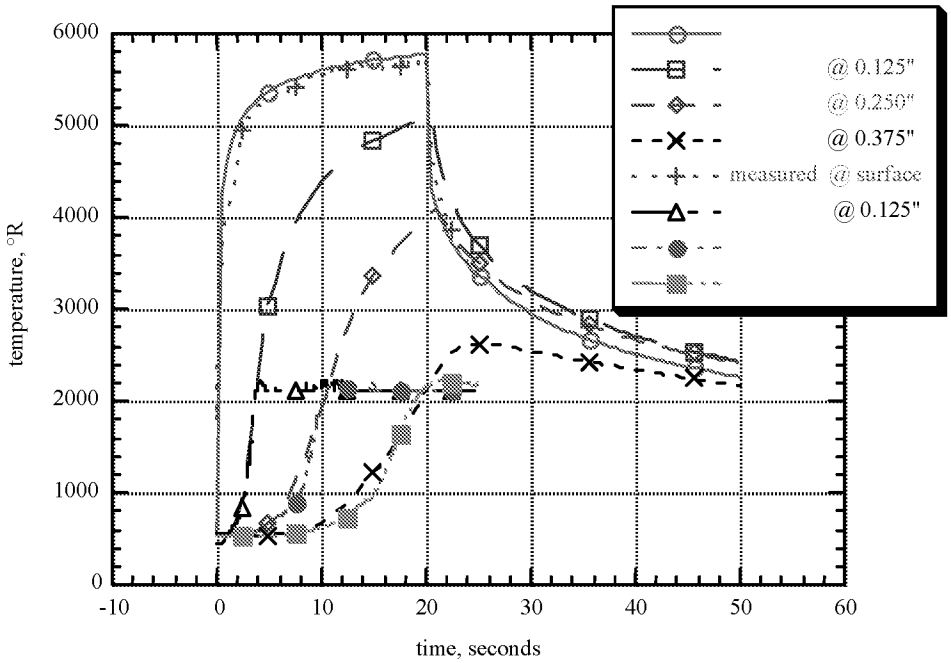

Fig. 16. Temperature Predicted Versus Measured Data
1000 Watt Case, 90° ply

CONCLUSIONS

Based on findings presented in this study the following conclusions are made:

1) Surface thermal simulation was best backfit by assuming a constant absorptivity and temperature dependent emissivity. At surface temperatures approaching 6000°R the two are equal at ~ 0.97 while at the lower temperatures, emissivity values were estimated to be ~ 0.85. It is recognized these backfit values are sensitive to the assumed radiometer values used during testing.

2) In-depth thermal response is not strongly dependent on detail calculation of the pyrolysis gas flow field. Somewhat satisfactory results have been obtained for years assuming gas flow is always directed to the heated surface and vapor condensation not a factor. The reason for the "weak" coupling is that in-depth thermal response is driven primarily by conduction into the material. Pyrolysis gas flow contributions to the overall energy balance are second order effects.

3) The trend of increasing total pressures with increasing surface heat rate is attributable to material "kinetic shift" meaning basically that at the higher heat rates, the material has a tendency to be less charred at higher temperatures. Trapped volatile's and initially evolved gases are dealing with higher temperatures and logarithmically smaller shifts in permeability thus pressure build up is greater.

4) Not accounting for pyrolysis gas reactions with carbon in the char layer seems to be a reasonable approximation at temperatures < 2000-2500°F. This premise is supported by findings presented by April[11] were specie concentration data was obtained for gas flow through char layers at various temperatures. Peak magnitudes of pyrolysis gas pressure build up, see Figs. 6-14, take place in partially decomposed material where local temperatures are in the 700-1100°F range. Water-carbon reactions within the char layer could potentially increase local permeability and thus affect pressure magnitude and distribution obtained from the global solution. The exact extent of influence is unknown at this time and suggest that permeability may be correlated versus actual material density rather than the degree of char parameter. This method of correlation could potentially capture the effect of residual char density changes due to heat rate dependence and/or enhanced pyrolysis gas reactions with carbon.

5) For a given heat flux, calculated gas pressures for ply angles less than 90° are greater than pressures calculated for the 90° case. This is a result of the across-ply permeability component coming into play in the effective 1-D property calculations, i.e., across-ply << in-plane permeability's at temperatures less than ~ 750°F. Gas generation rate is essentially unchanged while flow resistance has increased thus in-depth pressure build-up is greater. This trend is based on the premise that permeability is a function of degree of char only which is how the data was correlated in the thermal model. Its is known that permeability can be a function of compressive load which has the implications that the overall solution will necessarily have to couple thermal and structural response.

6) Formulation of the energy equation includes the local heat capacity of pyrolysis gas as contributing to the storage of energy in the material. The advective terms have always been included in CMA type codes but storage terms neglected on the premise of being second order. Results provided by the multi-specie calculations indicate that a liquid water-vapor mixture can exist during the decomposition process and that the mixture can be driven near critical conditions. In theory, a substance at the critical point has an infinite heat capacitance[12] and the asymptotes, near the singularity, are finite and are thermodynamically obtainable to a fixed extent. Historically, there has been a tendency to over predict in-depth temperature response using laboratory measured thermal properties. Many theories have been proposed to explain the differences which include kinetics, dynamic conductivity's, instrumentation, but it is believed by findings presented herein that part of the in-accuracy may be a result of not considering the thermodynamic state of water and implications of its pressure and temperature history.

REFERENCES

[1] Ross R., Strobel F., Fretter E., 1992, "Plasma Arc Testing and Thermal Characterization of NARC FM5055 Carbon-Phenolic", Document Number HI-046F1.2.9, Prepared For NASA Sponsored by the Solid Propulsion Integrity Program Nozzle work Package.

[2] Clayton J.L., 1992, "SINDA Temperature and Pressure Predictions of Carbon-Phenolic in Solid Rocket Motor Environment", in the Proceedings of the JANNAF Rocket Nozzle Technology Subcommittee Meeting, CPIA publication.

[3] Clayton F.I., 1992, "Influence of Real Gas effects on the Predicted Response of Carbon Phenolic Material Exposed to Elevated Temperature and Pressure Environments", in the Proceedings of the JANNAF Rocket Nozzle Technology Subcommittee Meeting, CPIA publication.

[4] Stokes Eric, 1997, "Room Temperature As-Cured In-Plane Permeability of MX4926 From Several Post Fired RSRM Throat Rings", Southern Research Corporation, SRI-ENG-97-281-9115.16

[5] Powers, Charles and Kendal, Robert, "Aerothermal Chemical Equilibrium Program (ACE)", May 1969, Aerotherm Corporation, Mountain Valley California

[6] Strobel, Forest and Ross, Robert, "CMA90S Input Guide and Users Manual, December 1990, Aerotherm Corporation, Huntsville Operations, Huntsville, Alabama

[7] Keyhani, Majid and Krishnan, Vikran, "A One-Dimensional Thermal Model with Efficient Scheme for Surface Recession", in the Proceedings of the JANNAF Rocket Nozzle Technology Subcommittee Meeting, CPIA publication, Mechanical And Aerospace Engineering Department University of Tennessee.

[7] Clayton , F.I., 1992, "Predictions of the Thermal Response of the SPIP 48-2 MNASA Ground Test Nozzle Materials", in the Proceedings of the JANNAF Rocket Nozzle Technology Subcommittee Meeting, CPIA publication

[8] Van Wylen and Sontag, " Introduction to Thermodynamics: Classical and Statistical" , John Wiley and Sons, Inc., 1970

[9] Bird, Stewart and Lightfoot, "Transport Phenomena", Department of Chemical Engineering, University of Wisconsin, John Wiley and Sons, Inc. 1960.

[10] Clayton , F.I., 1994, "Derivation of New Thermal decomposition Model For Carbon-Phenolic Composites", Science Applications International Corporation, DN. HI-065F/1.2.9, Contract Number NAS8-37801, Subtask:3.1.1.2

[11] April, G., Pike R. and Valle, E., "Modeling Reacting Gas Flow in the Char Layer of an Ablator", Louisiana State University, Baton Rouge, La., AIAA Journal Vol. 9, No. 6, June 1971

[12] Eckert, E.R.G. and Drake, R.M., "Analysis of Heat and Mass Transfer", Hemisphere Publishing Corporation, 1987